

Influence of Hydrodynamic Flow Patterns on the Corrosion Behavior of Carbon Steel in a Neutral LiBr Solution

Alvaro Soliz^{1,*}, Karl J.J. Mayrhofer², Luis Cáceres³

¹ Departamento de Ingeniería en Metalurgia, Facultad de Ingeniería, Universidad de Atacama, Av. Copayapu 485, 1532297 Copiapó, Chile

² Department of Interface Chemistry and Surface Engineering, Max-Planck-Institut für Eisenforschung GmbH, Max-Planck-Straße 1, 40237 Düsseldorf, Germany

³ Departamento de Ingeniería Química y Procesos de Minerales, Center for Biotechnology and Bioengineering, Universidad de Antofagasta, Av. Universidad de Antofagasta s/n, Antofagasta, Chile

*E-mail: alvaro.soliz@uda.cl

Received: 5 July 2018 / Accepted: 11 August 2018 / Published: 1 October 2018

The present study investigated the corrosion behavior of carbon steel samples using two electrochemical cell types that operate with distinctly different fluid flow patterns. For this purpose, an annular flow cell and a rotating disc electrode were used to investigate the influence of the immersion time on the corrosion kinetics of carbon steel in an aerated 0.5 M LiBr solution. The electrochemical results show good data reproducibility for both experimental cells. In both of these cells, the corrosion rate increases to a maximum value, and it gradually decreases with the immersion time. This shift in the corrosion rate is associated with a series of competing reaction mechanisms, which include a significant oxygen concentration reduction at the metal-solution interface, changes in the corrosion regime and oxide phase transformations. These competing reactions were described in terms of electrochemical kinetic parameters for partial reactions and equivalent circuits determined from polarization curves and electrochemical impedance spectroscopy measurements. The kinetic analysis shows that the oxygen reduction reaction is highly affected by the immersion time in solution, where non-realistic kinetic parameter values are found for long immersion times. Furthermore, the corrosion morphology found on the tested samples confirms the aggressive behavior of bromide ions, which promotes a pitting corrosion with a lateral spread of corrosion products.

Keywords: Carbon steel; Kinetic parameters; Pitting corrosion; Polarization

1. INTRODUCTION

In recent years, numerous studies have focused on the design and optimization of new electrochemical cells for the study of electrochemical phenomena. This research interest has promoted the development of new systems focused on the analysis, control, and prevention of the degradation of

materials caused by corrosion. However, the degradation of the properties of construction materials remains a crucial issue, and extensive research has been performed on this topic. Corrosion in highly aggressive electrolyte solutions in different experimental conditions is of special interest [1-4]. These conditions include different hydrodynamic patterns affecting mass transfer, the corrosion rate and/or passive film formation of various steel types [5, 6]. In this sense, an important consideration in the development of these new systems is the relationship between the geometrical arrangement of the electrochemical cell and the hydrodynamic conditions of the electrolyte, which allow reliable and reproducible experimental results to be obtained [7, 8].

Carbon steel is the most widely used steel material in engineering applications due its low cost and mechanical properties. Different works have examined the influence of the hydrodynamic behavior on the kinetics of carbon steel corrosion in different environments, including studies in either the presence or absence of a passive layer [5, 9, 10]. In our previous study [8], we presented a novel 3-electrode electrochemical flow cell containing a cylindrical band used as a working electrode (WE). This WE was inserted concentrically in the flow cell to form an annular space for the fluid flow such that its electrochemical behavior could be studied under different parametric conditions, such as solution flow rates. In addition to the hydrodynamic variables, the concentration of corrosive species and the immersion time are crucial factors for the evaluation of the corrosion reaction mechanism. Typically, the corrosion mechanism is characterized by a multi-stage oxide formation giving rise to many different situations with respect to the oxide layer composition and structure, as well as time evolution kinetics, and the mechanical degradation of the steel. Under certain conditions, the oxide layer structure provides corrosion resistance by inhibiting the mass and/or charge transfer through the oxide surface, where phase composition, morphology and the chemical composition of oxide films are also affected by the dissolved oxygen concentration in the electrolyte [11-13]. In aerated solutions, lepidocrocite ($\gamma\text{-FeOOH}$), maghemite ($\gamma\text{-Fe}_2\text{O}_3$) and hematite ($\alpha\text{-Fe}_2\text{O}_3$) are principally formed; however, in the absence of oxygen, the dissolution of iron to a magnetite oxide phase (Fe_3O_4) is predominant [14-19]. During the corrosion process in aerated solutions, the main electrochemical counterpart reaction to iron oxidation is the oxygen reduction reaction (ORR), which can be accompanied by the hydrogen evolution reaction (HER) from the reduction of water molecules in near neutral or alkaline solutions and at more negative potentials [8, 20, 21]. In particular, if the corrosion of carbon steel is cathodically controlled, then according to the mixed potential theory the ORR plays an important role in determining the corrosion rate [22-24]. As usually described in the literature, the ORR regime can be differentiated into a) a pure mass-transfer limited control, in which the corrosion rate is equivalent to the maximum current density known as the diffusion limiting current density, b) a pure charge transfer, i.e., kinetic control, in which the oxygen concentration in the bulk solution and metal surface are similar with a relatively low corrosion rate, and c) a mixed mass-charge transfer control, in which the corrosion rate is an intermediate value between situations a) and b) [8, 9, 25]. The ORR regime not only determines the corrosion rates but also the corrosion product stability and thus the secondary effects.

Due to its favorable thermophysical properties, lithium bromide has been widely used in absorption systems that are primarily composed of absorber, evaporator, generator and condenser stages. Careful attention should be taken for aqueous lithium bromide solutions, as they are corrosive,

especially if air is introduced into the solution; therefore, the various metallic parts that are in direct contact with these solutions, such as pipes, valves, fittings, pumps, and heat exchangers, will be severely affected by corrosion if no corrosion-preventive measures are considered. The performance of the absorption systems strongly depends on the thermodynamic properties of the working fluid, whereas the efficient operation and useful life depend principally on the corrosion rate. A particular aspect is the steel susceptibility to pitting corrosion caused by halide ions, which is reported in several studies [3, 4, 21]. The hydrodynamic influence on the corrosion rate, being an important operating factor in absorption systems, has received very little attention principally because of the complexity of the corrosion dependence on flow velocity and halide concentration.

In this work, the corrosion behavior of carbon steel AISI 1020 immersed in an aerated lithium bromide solution is studied at different immersion times by electrochemical methods and oxide characterization. We believe that experimental evidence of the corrosion behavior under different geometrical arrangements of electrochemical cells and electrode configurations is still limited. For this reason, in this study, two electrochemical cells with different geometrical configurations, a batch cell and a flow cell, were used. This study analyzes the influence of the fluid flow patterns on the corrosion rate of carbon steel and the kinetic regimes of the electrochemical partial reactions of hydrogen evolution, oxygen reduction and iron oxidation using the superposition model applied for experimental electrochemical data in relation to the iron oxide growth during the corrosion process, as well as the analysis of the influence of bromide ions on the metallic degradation type.

2. EXPERIMENTAL

2.1. Annular flow cell

Experimental measurements were performed using an annular flow cell (AFC) similar to that used in a previous work [8]. The hydrodynamic circuit consists of a centrifugal pump, a storage solution vessel, a flow cell and a flow-meter. The electrochemical system was a three-electrode cell with a working electrode made from carbon steel AISI 1020 bars, a counter electrode made from a pipe of stainless steel type 316L (internal diameter 10 mm) [8, 26], and a Ag/AgCl (KCl sat.) reference electrode. The working electrode was a cylindrical shaft containing a cylindrical band of carbon steel (diameter 5.5 mm and active area 86.39 mm²) attached at both ends to PVC adapters of the same diameter. The composite cylindrical shaft is situated concentrically in the flow cell, thereby forming an annular space through which the electrolyte solution circulates at a predetermined flow rate. In this cell configuration, the inner and outer walls of the annular cavity are the working and the counter electrode, respectively. These sections are intended for an entry zone 80 mm from the fluid inlet to approach a fully developed flow through the annular section. The storage solution vessel design allows a continuous gas to bubble through the electrolyte solution, leaving a bubble-free flow of solution.

2.2. Rotating disk electrode

A conventional three-electrode glass cell with a rotating disk electrode (RDE) system was used for the electrochemical measurements. The working electrodes were made from small cylindrical

carbon steel AISI 1020 bars (6 mm diameter and 10 mm length) that were inserted into a plastic rod (12 mm in diameter and 20 mm in length) and sealed by applying a resin adhesive, so that only the bottom planar surface (area 28.27 mm^2) was exposed to the test solution. A coil platinum wire and a Ag/AgCl (KCl sat.) electrode were used as the counter and reference electrodes, respectively.

A schematic representation of the electrochemical cells is shown in Fig. 1.

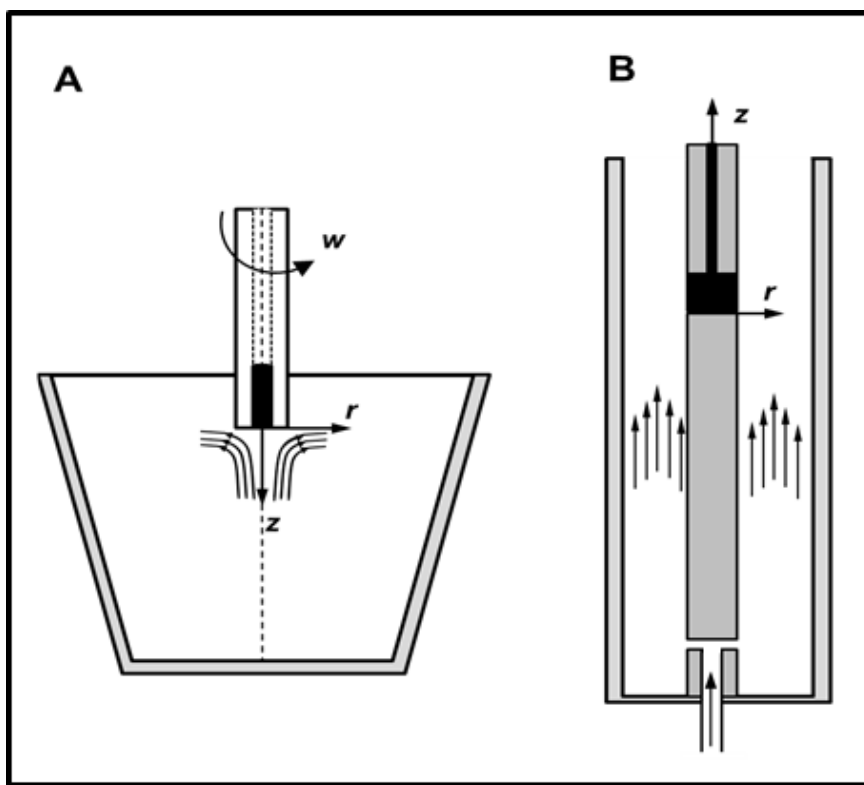


Figure 1. Schematic representation including a reference coordinate system and the flowing streamlines of the electrochemical batch and flow cells. A) Batch cell with rotating disk electrode and B) annular flow cell

2.3. Working electrodes and test solution

The test material used in all experiments was commercial carbon steel type AISI 1020, with a chemical composition (wt. %) of 0.2 C, 0.6 Mn, 98.5 Fe and traces of S, Si, Cu, Ni, Cr, Sn, P and Mo. Before each run, the working area was successively polished with SiC paper of 600 to 1200 grit, cleaned by an ultrasonic bath in ethanol for 5 min, washed with distilled water and immediately inserted in the electrolyte solution. All measurements were performed at room temperature ($22 \pm 0.5^\circ\text{C}$) in an unbuffered 0.5 M LiBr solution with volumes of 250 and 300 mL for the RDE and AFC, respectively. Analytical grade reagents from MERCK (MERCK-Germany) and distilled water were used to prepare the solutions. Changes in the bulk pH were registered via a pH-meter model F-71 LAQUA (HORIBA-Instruments). Prior to each experiment, air was bubbled in the bulk solution for 30 min to maintain a dissolved oxygen concentration of $7.3 \pm 0.1 \text{ mg L}^{-1}$, which was monitored using a dissolved oxygen meter HandyLab 680 (SI Analytics). For the deaerated experiments, the dissolved

oxygen in the electrolyte solution was purged by 30 min of nitrogen bubbling to obtain a residual dissolved oxygen concentration below 0.05 mg L^{-1} . The flow of air and nitrogen for aerated and deaerated solutions, respectively, was maintained throughout the experiments to maintain a constant dissolved oxygen concentration in the electrolyte solution.

The solution flow rate (q) and the rotation speed (w) for the AFC and RDE were 1.29 L min^{-1} and $2500 \text{ rev min}^{-1}$, respectively. The mean velocity values for the flow cell and for the batch cell were 0.39 and 0.78 m s^{-1} with calculated Reynolds numbers (Re) of 1960 and 2624, respectively. The values of the density and viscosity for a 0.5 M LiBr solution were taken from the literature [21].

2.4. Electrochemical measurements

For the electrochemical measurements, a Biologic SP-150 potentiostat controlled by EC-Lab software was used as an electrochemical interface. All potentials reported in this work were adjusted to the standard hydrogen electrode (SHE). Measurements of the open circuit potential (OCP) were performed for 300 min starting immediately after the immersion of the working electrode in the test solution. Electrochemical measurements were performed using the linear sweep voltammetry (LSV) technique, which was scanned in the anodic direction at a low scan rate of 1 mV s^{-1} , to obtain a quasi-steady state condition. Electrochemical impedance spectroscopy (EIS) measurements were conducted at the open circuit potential using an AC signal with 10 mV of amplitude over a frequency range of 100 kHz to 50 mHz .

2.5. Estimate of the kinetic and corrosion parameters from polarization data

To obtain a better understanding of the carbon steel corrosion behavior in LiBr aqueous solution, a kinetic analysis of the partial anodic and cathodic reactions are discussed in the context of the mixed potential theory. This theory assumes that the net current density is given by a linear superposition of the total current densities of each of the electrochemical partial reactions in the framework of the principle of electric charge conservation. Assuming that each partial reaction occurs on the same surface area, this principle can be expressed as [8, 9, 22-24]:

$$i = i_{Fe} + i_{O_2} + i_{H_2} \quad (1)$$

Anodic region:



$$i_{Fe} = i_{0,Fe} \exp\left(\frac{2.303\eta_{Fe}}{b_{Fe}}\right) \quad (3)$$

Cathodic region:



$$i_{H_2} = i_{0,H_2} \exp\left(\frac{2.303\eta_{H_2}}{b_{H_2}}\right) \quad (5)$$



$$i_{O2} = i_{0,O2} \exp\left(\frac{2.303\eta_{O2}}{b_{O2}}\right) \left(1 - \frac{i_{O2}}{i_{l,O2}}\right) \quad (7)$$

where $i_{0,j}$ is the exchange current density, b_j is the Tafel slope, $\eta_j=E-E_{eq,j}$ is the overpotential, $i_{l,j}$ is the limiting current density, and $E_{eq,j}$ is the equilibrium potential, with subscript j designating iron oxidation, hydrogen evolution and the oxygen reduction reaction, respectively. Values taken for the calculation of equilibrium potentials were; 1×10^{-6} M for the ferrous ion concentration, 7.3 mg L $^{-1}$ for the dissolved oxygen concentration, a temperature of 22 °C, and an initial pH of 6.9 . Equilibrium potentials of -616 , 827 and -392 mV_{SHE} for iron oxidation, oxygen reduction and the hydrogen evolution reaction, respectively, were determined.

The proposed partial reactions are based on extensive previous investigations concluding that in alkaline and near-neutral aerated solutions, the main reaction that counterbalances the iron oxidation corresponds to the oxygen reduction reaction and to a minor extent to the hydrogen evolution reaction [9, 20, 21]. The electrochemical corrosion parameters included in Eqs. 3, 5 and 7 were obtained following a procedure described in our previous reports [8, 21] assuming a kinetic mechanism based on a pure charge transfer control for the HER and iron oxidation, and a mixed charge transfer-diffusion control for the ORR [9, 20].

Corrosion potentials E_{corr} and corrosion current density i_{corr} values were obtained for a null net current density (i.e., $i=0$ A m $^{-2}$) applied for the partial polarization curves: $i_{corr}=i_{Fe}=|i_{O2} + i_{H2}|$ [23, 24].

2.6. Surface analysis

The corrosion products deposited on the metallic surface after the experimental measurements were characterized at room temperature via Raman spectra using a Horiba Jobin LabRAM confocal Raman microscope with 50x magnification, and X-ray diffraction using a Shimadzu XRD-6100 diffractometer. The morphology of the corroded surface was examined using a scanning electron microscope (SEM) Zeiss EVO MA 10 and an optical microscope Olympus BX 41M. For this propose, the oxide layer deposited on the metallic surface was removed in an ultrasonic bath by immersion of the working electrodes in a 5% citric acid solution.

3. RESULTS AND DISCUSSION

3.1. Open circuit potential measurements

Fig. 2 shows open circuit potential (OCP) time profiles recorded for carbon steel electrodes in unbuffered 0.5 M LiBr solution using RDE and AFC electrochemical cell configurations. For comparison purposes, OCP measurements were also performed in deaerated solutions in an RDE under similar conditions. For the RDE in aerated solution, this measurement presents different variation

patterns, starting with an OCP decrease from -200 mV_{SHE} to a local minimum value of -207 mV_{SHE} up to approximately 70 s followed by a shift to more positive values up to -203 mV_{SHE} (Fig. 2 inset) and, finally, an asymptotic trend toward a steady value of -347 mV_{SHE} after 233 min of immersion in the test solution.

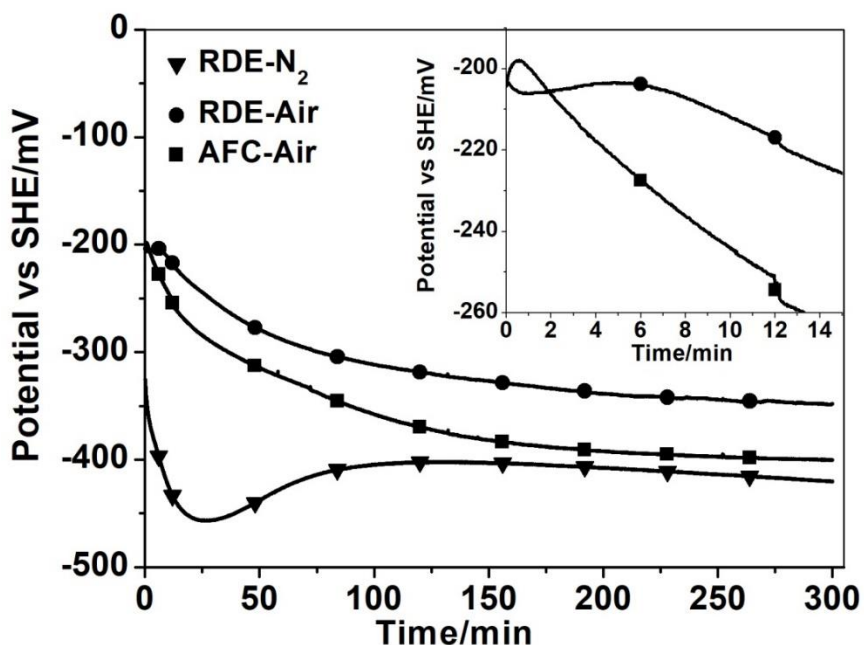


Figure 2. OCP-time profiles of carbon steel electrodes during 300 min of immersion in aerated (air) and deaerated (N_2) 0.5 M LiBr solution measured in AFC and RDE cells



Figure 3. Images of carbon steel electrodes after 300 min of immersion at the OCP in aerated 0.5 M LiBr solution. Annular flow cell (left) and rotating disk electrode (right)

In contrast, for the OCP measurement using the AFC with a constant inlet velocity, the initial

OCP decrease is absent, and the maximum value presents a time shift of 60 s ahead of the maximum of that of the RDE with an asymptotic trend towards a steady value of -354 mV_{SHE} after 233 min of immersion. During the first minutes of immersion, the fluctuations in the OCP are attributed to the aggressive attack of bromide ions, which can be explained in terms of competing metal dissolution reactions, and the subsequent pitting formation and growth, in addition to the surface precipitation of hydrous oxides [1-3]. As a result of this competition between reactions at the surface free of a protective layer, a non-steady state is attained for the OCP values in the first minutes of immersion, where three stages can be identified, pit nucleation, growth and re-passivation [13, 27, 28]. Fig. 3 shows signs of oxides covering the metal surface under RDE and AFC conditions after 300 min of exposure; it is presumed that at this stage pit nucleation can occur only under the influence of spreading oxides that emerge from growing pits. As the metallic corrosion progresses with immersion time, the subsequent OCP variations can be attributed to diffusion of bromide ions through the channels of the surface porous oxide layer, which is also accompanied by the forced convection condition represented by different flow streamline patterns, as shown in Fig. 1. A visual appreciation of the effect of streamlines representing different hydrodynamic conditions between the AFC and RDE is confirmed by the axial and spiral patterns of the oxides, respectively (Fig. 3).

These situations related to the hydrodynamic regime and the oxide layer coverage may explain the lower OCP values exhibited by the carbon steel in the AFC cell compared to that in the RDE cell, where a lower flow velocity of solution around the electrode causes a driving force for the ORR, promoting a lower dissolved oxygen concentration near to the diffusion boundary layer. Furthermore, the OCP values exhibited by carbon steel are significantly different in deaerated solutions compared with aerated solutions, indicating a HER favored reaction associated with the nucleation and pitting formation processes that occur on a bare metal surface [8, 29, 30]. This period in the deaerated solution is expressed by a shift to more negative values of the OCP during the first 25 min, where the HER occurs in conjunction with the nucleation and pitting formation, followed by a slight shift to more positive values of the OCP due to the iron oxide transformation at near neutral pH, to finally reach a steady state after 80 min of immersion due to a passive condition with the formation of magnetite from ferrous hydroxide according to the Schikorr reaction [31].

Carbon steel corrosion (initially free of oxide) during the early time of immersion, where iron is oxidized to dissolved Fe⁺² species, is followed by a fast hydrolysis and further formation of ferrous hydroxide Fe(OH)₂ [14, 31-33]. Depending on the electrolytic solution, the bulk pH and the rate of oxygen transfer to the metallic surface, this ferrous hydroxide is thermodynamically unstable and will be hydrated or oxidized to another oxide such as lepidocrocite (γ -FeOOH), magnetite (Fe₃O₄) or hematite (Fe₂O₃) [14, 31, 34, 35]. In addition, magnetite is very sensitive to oxidation and can be transformed to maghemite (γ -Fe₂O₃) in the presence of oxygen [33]. Previous studies made by Stratmann and co-workers [36] indicate that the formation of magnetite starts at potentials between -0.3 and -0.4 V_{SHE} at the near neutral pH of 6 with kinetics sensitive to an increase in Fe⁺² ions. Then, the temporal evolution of OCP characterized by a continuous decrease would indicate the formation of different oxide phases deposited on the metallic surface. According to the temporal changes of the bulk pH shown in Fig. 4 and measured during the potentiodynamic measurements, the pH values were 7.1 and 6.8 for the AFC and RDE, respectively. According to these values, the formation of a lepidocrocite

γ -FeOOH phase would be dominant during the first 60 min of immersion, followed by the formation of a new phase of magnetite F_3O_4 at longer immersion times and potentials more negative than -300 mV_{SHE}, which will be associated with a low dissolved oxygen concentration near the metallic surface and the further reaction of ferrous ions with a previously formed lepidocrocite phase [31, 35-37].

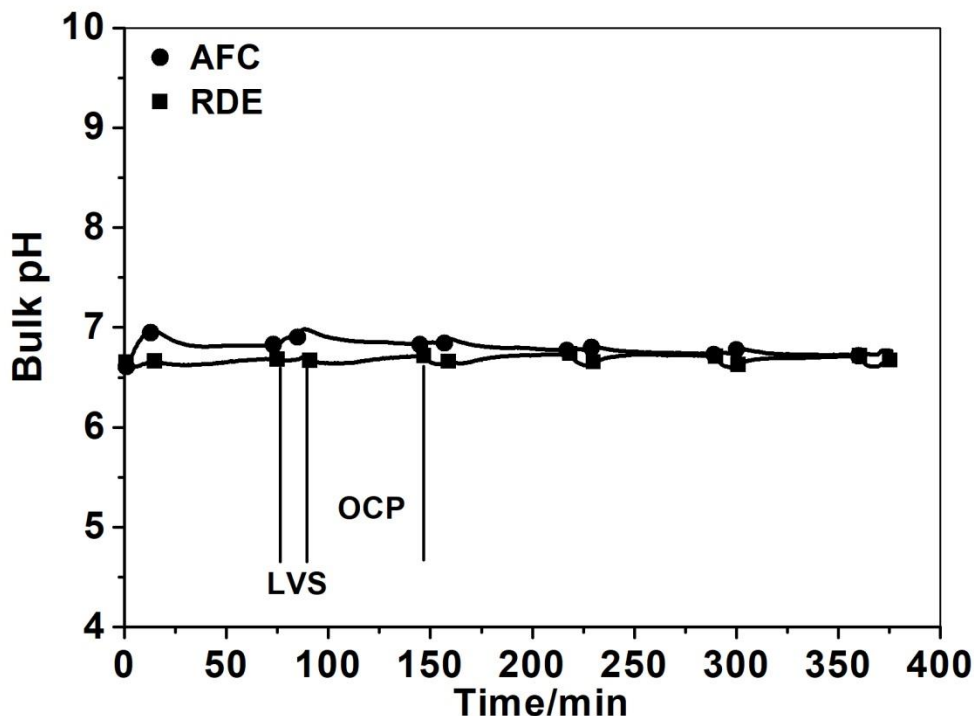


Figure 4. Time variations of the bulk pH during OCP and LVS measurements of carbon steel in aerated 0.5 M LiBr solution

3.2. Analysis of the corrosion products

Fig. 3 shows macro photos of corroded carbon steel samples after completing the OCP measurements. A visual inspection of the corroded samples shows a compact deposit of corrosion products (iron oxides) on the metallic surface with a pattern distribution that depends on the flow streamlines, either in the direction of rotation or the axial direction for the RDE and AFC, respectively. The visual inspection also reveals that this oxide-film consists of a two-layer structure, an inner black solid phase and an outer orange phase. As previously mentioned, the oxide phases are primarily composed of magnetite and lepidocrocite in the inner and outer layers, respectively [18]. To confirm the structure of the oxide phases deposited by the corrosion process, the specimens were subjected to Raman spectroscopy and X-ray diffraction analysis and their spectra are shown in Fig. 5. For the Raman spectroscopy analysis obtained near the orange and black oxide layers, characteristic peaks are observed at 1312, 380 and 251 cm^{-1} indicating the presence of a γ -lepidocrocite structure [15-17]. Other intense peaks are observed at 422 and 670 cm^{-1} , which can be attributed to a magnetite structure [16, 17, 37]. An additional peak of lower intensity was observed at 500 cm^{-1} that indicates the presence of maghemite [16, 17, 31]. The X-ray diffraction analysis confirms that the deposited corrosion products are composed principally of a magnetite and γ -lepidocrocite oxides phase. Under these

considerations, it is possible to assess that the inner oxide layer composed of magnetite may act as the protective layer that limits the diffusion of oxidative species up to the metallic surface, thus retarding the corrosion process. Yamashita [39] reported similar results for steel samples exposed for a long period under industrial atmospheres, with a rust layer composed of one or more alternating layers of goethite and lepidocrocite and patches of maghemite and/or magnetite.

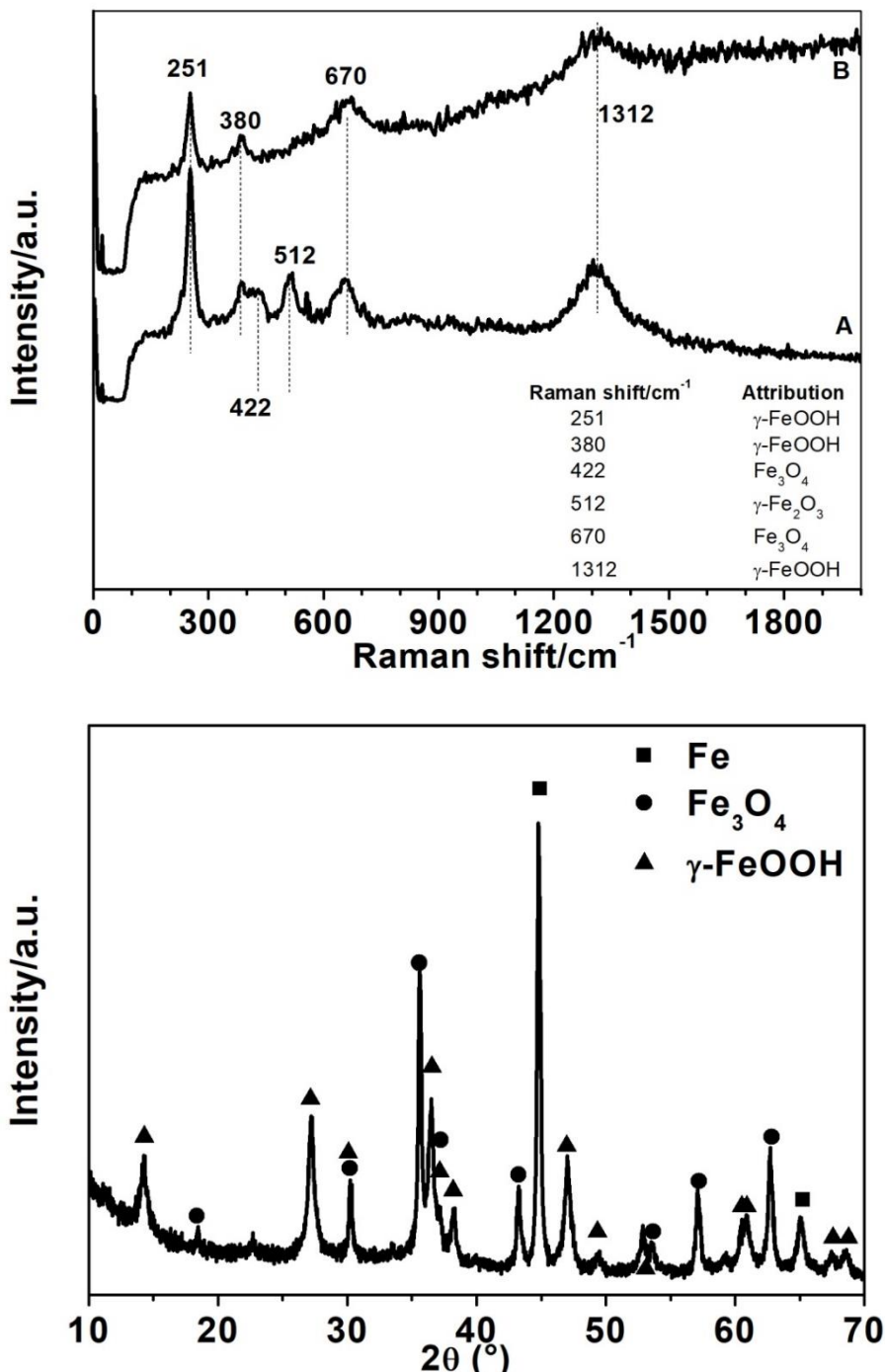


Figure 5. Raman spectra (top) and X-ray diffraction (bottom) patterns of corrosion products formed on the carbon steel surface after 300 min of immersion at the OCP in aerated 0.5 M LiBr solution. Raman spectra of the black oxide phase (A) and orange oxide phase (B)

3.3. Linear sweep voltammetry measurements

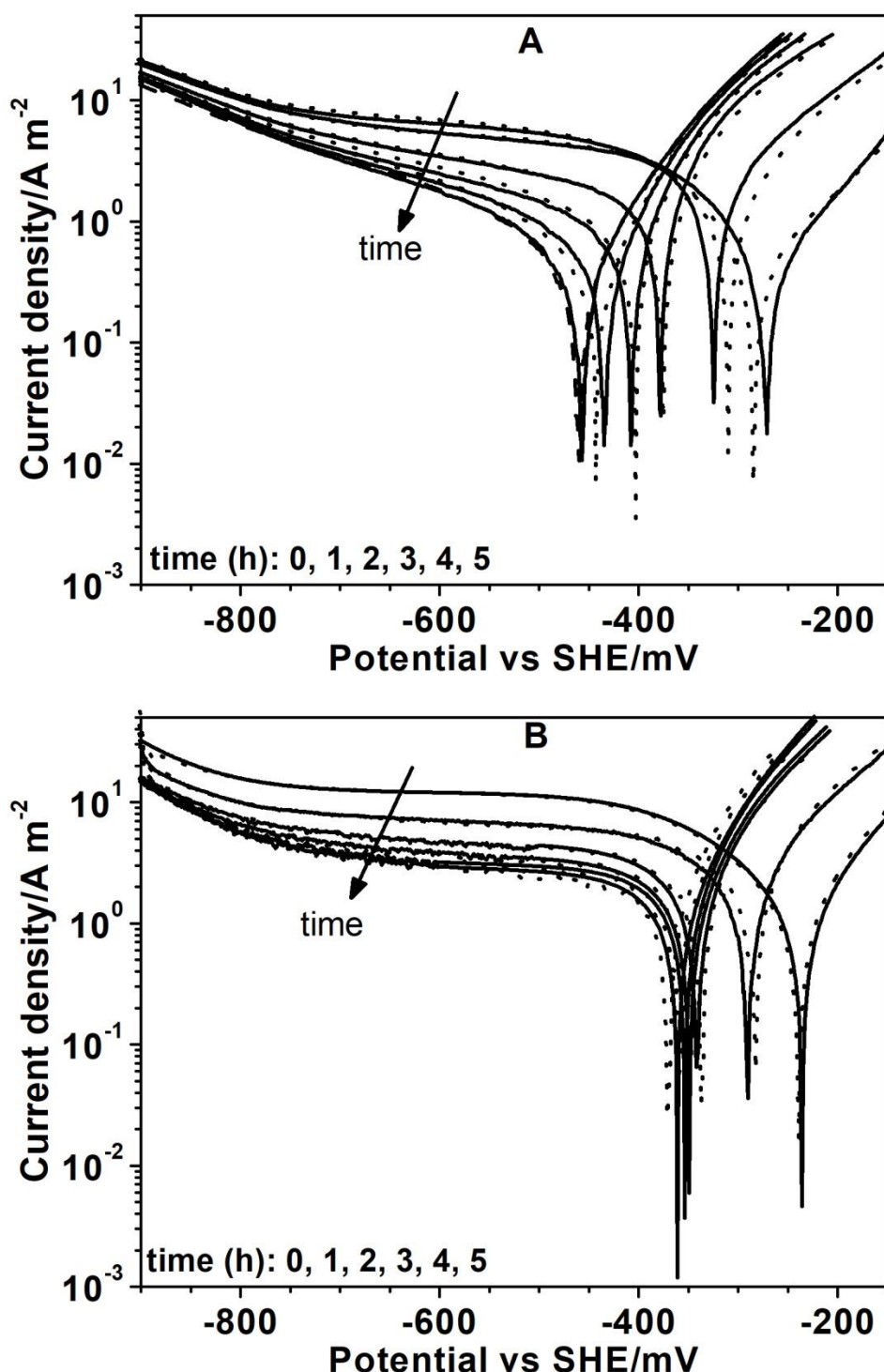


Figure 6. Succession of measured polarization curves at 1-hour intervals during 5 h of immersion of carbon steel in aerated LiBr 0.5 M. A) AFC, and B) RDE. 2nd sequential cycles are dotted lines. The scan rate is 1 mV s⁻¹

The experimental polarization curves of carbon steel in aerated 0.5 M LiBr solution were obtained at different immersion times using the AFC and RDE. The corrosion time evolution was examined over 5 hours through a series of polarization curves measured at intervals of one hour after

an OCP condition on the same electrode. All experiments were repeated for both electrochemical cells to verify the reproducibility of the results, as shown in Fig. 6. For the RDE it is interesting to note that during the first two hours of immersion the polarization curves present good data reproducibility followed by slight deviations at longer immersion times, where the inversion potential from the cathodic to the anodic branch is principally affected. In contrast to the RDE results, the variations in the data reproducibility for the AFC indicate a slight shift of the inversion potential during the first hours of immersion, which is minimized at longer immersion times.

Table 1. Electrochemical parameters for carbon steel electrodes immersed in aerated 0.5 M LiBr solution using the AFC and RDE at different immersion times. Average values (Error %)*

Parameter	Rotating Disk Electrode					
	0 h	1 h	2 h	3 h	4 h	5 h
E_{corr}^{**} (mV _{SHE})	-242(1)	-288(2)	-342(1)	-352(4)	-355(2)	-367(9)
i_{corr} (A m ⁻²)	1.69(0.4)	5.16(0.3)	4.33(0.1)	3.50(0.5)	3.04(0.2)	2.68(0.02)
$-i_{l,O2}$ (A m ⁻²)	1.70×10^{-8} (0.2)	4.69×10^{-10} (0.5)	1.84×10^{-14} (0.02)	1.18×10^{-24} (0.1)	7.48×10^{-29} (0.5)	3.30×10^{-33} (0.6)
$-i_{l,H2}$ (A m ⁻²)	9.65×10^{-3} (1.2)	1.03×10^{-2} (0.4)	8.33×10^{-3} (0.3)	8.90×10^{-3} (0.6)	8.39×10^{-3} (0.1)	1.01×10^{-2} (0.2)
$i_{l,Fe}$ (A m ⁻²)	2.49×10^{-3} (1.3)	7.82×10^{-2} (1.0)	4.59×10^{-2} (0.2)	2.94×10^{-2} (1.7)	1.06×10^{-2} (0.7)	1.39×10^{-2} (8.9)
$-b_{O2}$ (mV dec ⁻¹)	132(0.013)	104(0.025)	75(0.047)	45(0.1)	39(0.1)	34(0.2)
$-b_{H2}$ (mV dec ⁻¹)	156(0.8)	162(0.05)	161(0.1)	163(0.3)	161(0.2)	165(0.1)
b_{Fe} (mV dec ⁻¹)	132(0.1)	181(0.1)	139(0.1)	127(0.5)	107(0.7)	109(0.3)
$ i_{l,O2} $ (A m ⁻²)	11.99(0.4)	6.70(0.9)	4.69(0.2)	3.60(0.3)	3.09(0.8)	2.78(0.1)
$K=1-i_{corr}/i_{l,O2} $	0.86	0.23	0.08	0.03	0.02	0.04
Annular Flow Cell						
Parameter	0 h	1 h	2 h	3 h	4 h	5 h
E_{corr}^{**} (mV _{SHE})	-270(4)	-318(14)	-376.5(7)	-407.5(7)	-442.5(7)	-459.5(1)
i_{corr} (A m ⁻²)	0.72(1.4)	2.80(2.7)	2.42(0.8)	1.81(0.4)	1.42(1.3)	1.16(1.2)
$-i_{l,O2}$ (A m ⁻²)	3.09×10^{-9} (0.5)	1.77×10^{-13} (3.4)	1.91×10^{-40} (1.1)	3.27×10^{-51} (0.8)	3.28×10^{-58} (0.4)	1.60×10^{-54} (1.5)
$-i_{l,H2}$ (A m ⁻²)	0.06(1.2)	0.09(1.5)	0.16(1.7)	0.15(0.02)	0.16(0.26)	0.12(2.6)
$i_{l,Fe}$ (A m ⁻²)	3.85×10^{-3} (0.9)	5.01×10^{-2} (1.0)	3.77×10^{-2} (0.5)	3.96×10^{-2} (0.3)	8.35×10^{-2} (2.7)	8.99×10^{-2} (0.6)
$-b_{O2}$ (mV dec ⁻¹)	131(0.1)	84(0.2)	29(0.06)	23(0.02)	20(0.0)	22(0.1)
$-b_{H2}$ (mV dec ⁻¹)	211(0.03)	230(0.4)	258(0.6)	258(0.2)	260(1.2)	249(0.7)
b_{Fe} (mV dec ⁻¹)	150(0.1)	172(2.1)	133(0.02)	128(0.2)	141(0.3)	140(0.1)
$ i_{l,O2} $ (A m ⁻²)	6.05(1.2)	4.60(0.7)	2.58(0.7)	1.63(0.1)	1.15(1.2)	0.97(1.7)
$K=1-i_{corr}/i_{l,O2} $	0.88	0.39	0.06	-0.11	-0.24	-0.2

* Error values were calculated as the difference between replicate values divided by the average value. The % error values are in parenthesis.

** Error unit in mV

The polarization curves show typical shapes for carbon steel in aerated solutions [8, 9, 19] which theoretically are a result of a mixed contribution from the partial reactions of iron oxidation,

dissolved oxygen reduction, and hydrogen evolution. The formation of a planar plateau at intermediate potentials followed by a rapid increase in the current density at high negative potentials corresponds to the ORR and HER, respectively. This last reaction was visually confirmed from the generation of microbubbles on the metallic surface during the potential sweep at negative potentials. The kinetic and corrosion parameters were obtained by non-linear regression of Eq. 1 in terms of the mixed potential theory and are presented in Table 1.

The values are expressed as the average of two independent polarization curves. A common feature in all polarization curves in the cathodic branch is a progressive current density decrease with an intermediate planar plateau, which converges to zero net current density at the corrosion potential. The intermediate planar plateau indicates that the ORR is controlled by a diffusion regime expressed in terms of the limiting current density that persists up to the corrosion potential value. Additionally, the decrease in the cathodic current density near to the corrosion potential indicates that the ORR is controlled by a mixed diffusion and charge regime.

Despite these common features, each curve has a distinct particularity with the immersion time. For the AFC, the anodic branch shows a marked increase in current density values for up to 2 hours followed by a nearly unchanged condition. In contrast, the RDE anodic branch increased at a nearly constant rate throughout the 5 hours of measurements. Moreover, although a decreasing cathodic plateau is observed for both electrochemical cells, its extent persisted for a wider potential range for the RDE cell compared with the AFC cell. Consequently, the limiting cathodic slopes of each curve are more closely aligned in the AFC cell.

The corrosion of carbon steel in aqueous solutions is conducted by electrochemical processes consisting of a set of partial reactions, each with a complex combination of steps that can be simplified for a kinetic rate estimate assuming the existence of a single controlling step [9, 18, 31, 33]. The linear behavior of the anodic branch shown in the Tafel polarization curves (Fig. 6) and the presence of pits visually observed under the oxide layer (Fig. 11) indicate that iron oxidation gradually changes from uniform dissolution to a localized corrosion where the iron oxidation predominantly occurs inside the pits, while they are covered by a porous oxide layer that allows ion mobility. In general, it is accepted that metastable pits can be initiated at potentials below those required for stable pits where a deviation from the Tafel line is evidenced; such a deviation is only noticeable at the first polarization curve measured in the AFC cell. Thus, the oxidation rate should be a diffusion controlled process through the porous oxide layer covering the pits. Given that this oxide layer is not at equilibrium, the point defect model (PDM) cannot be invoked here to explain the charge mobility through this layer [40, 41]. In these terms, the Tafel slope could represent a charge transfer process occurring either within the porous oxide layer or on its external surface.

Furthermore, the b_{Fe} values of the Tafel slopes, which were maintained from 100 to 180 mV dec⁻¹ for both electrochemical cells, are similar to the data reported in the literature for carbon steel and iron exposed to high saline solutions [4, 8, 40, 41]. This suggests that in 5 hours under aerated conditions the Tafel slope for iron oxidation reflects a kinetic mechanism that is slightly affected by the immersion time and the type of the hydrodynamic regime. A supporting fact for the role of the oxide film in the iron oxidation mechanism is the significantly lower b_{Fe} value of 60 mV dec⁻¹ reported for iron in deaerated solutions, in comparison with those in aerated solutions [4, 34, 42, 43]. Other

main factors affecting iron oxidation are the bulk pH of the solution and the presence of high salt concentrations in solution [4, 8, 42, 21]. As no appreciable changes were observed in bulk pH (Fig. 4), the anodic Tafel slope variation can be explained in terms of the coverage surface due to the adsorption of bromide ions, oxygen molecules and/or complex species from the oxidation process. Notably, this range of b_{Fe} values is larger than those values reported for NaCl solutions [21], indicating a greater adsorption of bromide ions on the metallic surface caused by diffusional transport. The maximum intermediate b_{Fe} and i_{corr} values observed for the AFC and RDE cells at one hour of immersion could be a manifestation of competing processes of nucleation and pitting propagation, in addition to a passivation process and the formation of the iron oxide layer on the metallic surface, as shown in Fig. 3.

To show how the immersion time affects the HER, the partial cathodic curves are analyzed in terms of the Tafel slope and the exchange current density values that are tabulated in Table 1. From Fig. 6 it is found that at -750 mV_{SHE} the net current density decreases with the immersion time, which can be attributed at a first instance to decreasing HER kinetics. However, it must be noted that the kinetic parameters b_{H2} and $i_{0,H2}$ maintain fairly constant values with immersion time (Table 1) indicating a constant hydrogen evolution rate for both electrochemical cells. Thus, the observed decrease in the absolute current density with immersion time is only due to changes in $|i_{t,O2}|$ as a result of an increasing oxygen mass transfer resistance from a growing oxide film thickness. Additionally, from the $i_{0,H2}$ and b_{H2} values, larger i_{H2} values for AFC in comparison with RDE are observed. This result is compatible with the temporal changes in the OCP, where a tendency to larger positive potentials was observed in the RDE, due to the fast formation of the corrosion products.

As previously mentioned, the kinetic behavior of the partial ORR represented as Eqs. 1 and 7 follows a mixed charge-transfer and diffusion control regime. Accordingly, the variations of the kinetic parameters are sensitive to synergistic changes between the oxygen concentration, the predominant hydrodynamic regime and the oxide film evolution over the metallic surface. Such considerations are compatible with changes in the kinetic parameters observed in Table 1 and Fig. 6. For instance, the initial $-b_{O2}$ values of the RDE and AFC are 132 and 131 mV dec⁻¹, respectively, but abruptly become substantially different after 2 hours of immersion due to a drop in the $-b_{O2}$ value of the AFC from 84 to 22 mV dec⁻¹. At longer immersion times, this difference decreases as all $-b_{O2}$ values are lower than 35 mV dec⁻¹. These parameters suggest that the ORR regime transforms from a mixed control regime to a pure diffusional control regime during the first two hours of immersion.

This is corroborated by the unrealistic $-i_{0,O2}$ values (1×10^{-20} to 1×10^{-55} A m⁻²) observed at immersion times longer than two hours.

The $-i_{0,O2}$ parameter, which indicates how fast the redox (oxygen-reduction) reactions occur at equilibrium, exhibits a marked decrease with time, particularly for the AFC cell. The $-i_{0,O2}$ values under an initial oxide-free surface condition are similar for both electrochemical cells, and also agree with previous reports on carbon steel in diluted LiBr solutions [21].

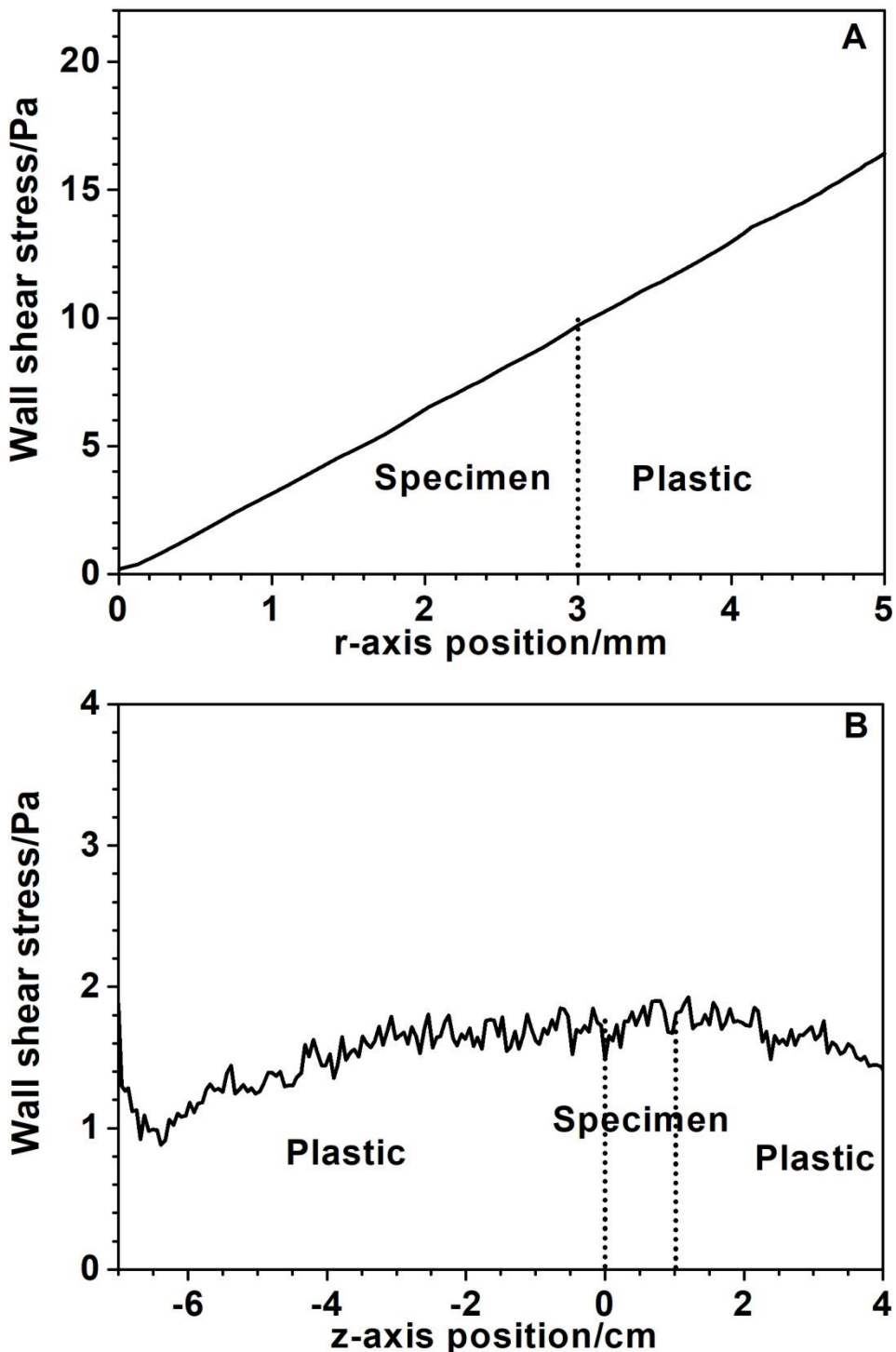


Figure 7. Computational simulation of the fluid flow distribution. Wall shear stress across the wall surface of the A) RDE and B) AFC

At long immersion times, $-i_{l,O_2}$ diminishes to negligible values of 1.60×10^{-54} and $3.30 \times 10^{-33} \text{ A m}^{-2}$ for the AFC and RDE, respectively. This is visually appreciated in Fig. 6 as a polarization curve tendency with time toward a typical oxygen-free behavior, as shown in a previous study [8].

The larger $|i_{l,O_2}|$ values observed for the RDE compared to the AFC seem to contradict the abovementioned implication of a larger amount of oxides in the AFC cell inferred from a larger $-i_{l,O_2}$

drop for AFC. This could imply that iron oxide detachment is more intense for RDE due to a larger wall shear stress exerted on an RDE in comparison to an axial flow in an AFC. This statement can be supported through a hydrodynamic characterization based on a computational fluid dynamic (CFD) simulation for the AFC and RDE. Appendix A presents a hydrodynamic characterization of the RDE and AFC by solving the Navier-Stokes equations under a steady state and similar conditions to our previous work [42]. In Fig. 7, the wall shear stress profiles for both electrochemical cell configurations and hydrodynamic conditions are shown. According to the numerical simulation, it is observed that for the RDE, a maximum wall shear stress of approximately 9.7 Pa is at 3 mm from the end of the specimen, and a value of 1.82 Pa is observed for the AFC over the length of the specimen. Thus, the results can be related to an oxide detachment from the metallic surface that becomes more intense for the RDE compared to the AFC.

In the following section, we will discuss the $|i_{l,O_2}|$ values at different immersion times. Table 1 shows that $|i_{l,O_2}|$ decreases with immersion time for the AFC and RDE cells, but is larger for the RDE case. The reason for this behavior can be explained in terms of the dependence of $|i_{l,O_2}|$ on the mass transfer from the hydrodynamic regime and the precipitation of corrosion products on the solid surface that restricts the dissolved oxygen diffusion through the concentration boundary layer. The influence of the hydrodynamic flow on the oxygen diffusion has been analyzed for different geometries, e.g., Levich's [22] and Ghosh and Upadhyay's [44] equations for the RDE and AFC, respectively. In both equations, the limiting current density is directly proportional to the dissolved oxygen concentration and to $w^{0.5}$ for the RDE [22] and to $Re^{1/3}$ for the AFC [44]. Next, under fixed hydrodynamic conditions the decrease in $|i_{l,O_2}|$ with the immersion time is only due to the surface oxide layer growth, which restricts the oxygen mass transfer to the metal surface. Thus, the mass transfer resistance for the limiting current density $|i_{l,O_2}|$, defined as a reciprocal value of the overall mass transfer coefficient, has two serial resistance terms. The first one, which is fixed, is due to the hydrodynamic boundary layer, and the second one is a variable resistance that increases with oxide layer growth. In this context, the larger experimental $|i_{l,O_2}|$ values (Table 1) for the RDE can be interpreted as a lower mass transfer resistance for the fixed term in comparison with the AFC cell due to differences in the hydrodynamic regimes.

3.4. Variational patterns for corrosion current densities and potentials

The influence of immersion time on the corrosion current density and corrosion potential is shown in Fig. 8. The E_{corr} and i_{corr} values of both electrochemical cells show a similar tendency with immersion time. The corrosion potential shifts toward negative potentials with immersion time, which is a direct consequence of the decreasing trend of $|i_{l,O_2}|$ under the condition $i_{O_2} + i_{H_2} + i_{Fe} = 0 \text{ A m}^{-2}$.

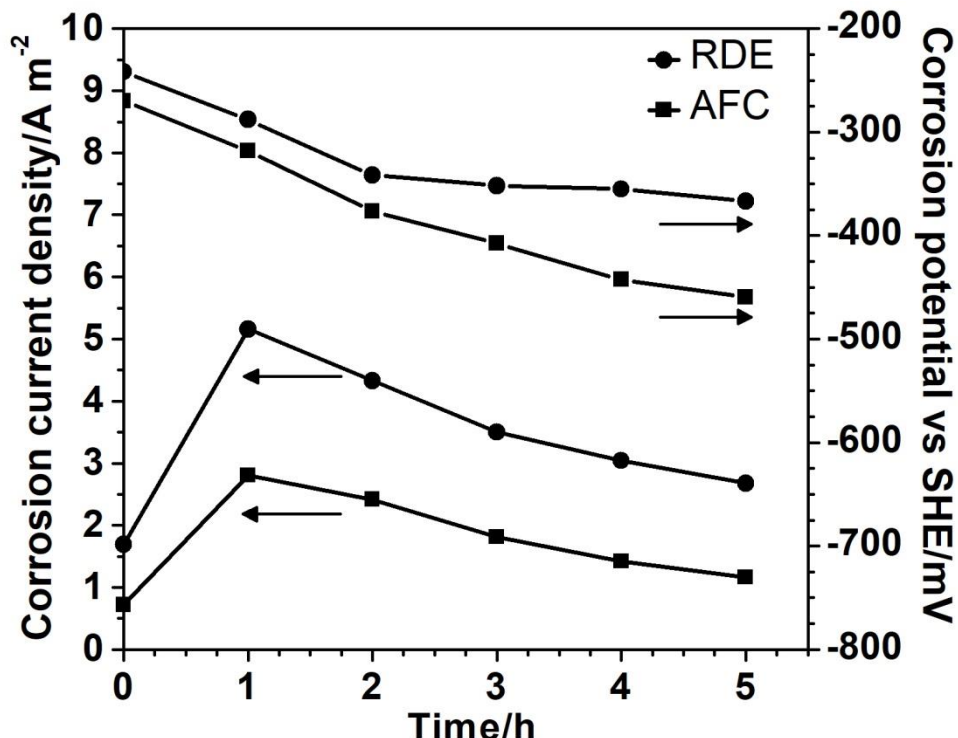


Figure 8. Variation of corrosion current density and corrosion potential with immersion time for carbon steel in an aerated 0.5 M LiBr solution in an RDE and AFC

As expected, these results correspond with OCP measurements and with a previous work related to the hydrodynamic influence on the corrosion behavior of carbon steel in deaerated and aerated solutions [8]. In that work, it was found that in reference to a polarization curve measured in flowing aerated solutions, E_{corr} was progressively shifted towards more negative values for stagnant aerated and flowing deaerated solutions, respectively.

Initially, the corrosion rate increased during the first hour of immersion, reaching maximum values of 5.16 and 2.8 A m⁻² for the RDE and AFC, respectively, followed by a continuing asymptotic decrease at longer immersion times. To obtain a good understanding of the underlying corrosion regimen and the effect of oxygen mass transfer on the mixed-control kinetics of the ORR, the parameter $K=1-i_{corr}/i_{l,O_2}$ was used as an index that expresses the degree of incidence of the diffusion regime at a corrosion condition. As shown in Table 1, this parameter depends significantly on the immersion time, which is characterized by initial values close to 1 (a controlling condition of the pure charge-transfer regime for ORR), that decrease progressively at long exposure times, where a major incidence of the diffusion regime can be observed [8, 23]. The negative K values indicate large i_{H_2} values that are naturally expected at more negative potentials. In this respect, it is interesting to note that negative values for K are only observed in AFC experiments where the E_{corr} values are more negative than those of the RDE. A schematic representation of the partial polarization curves and the changes in the regime control during the corrosion process are depicted in Fig. 9.

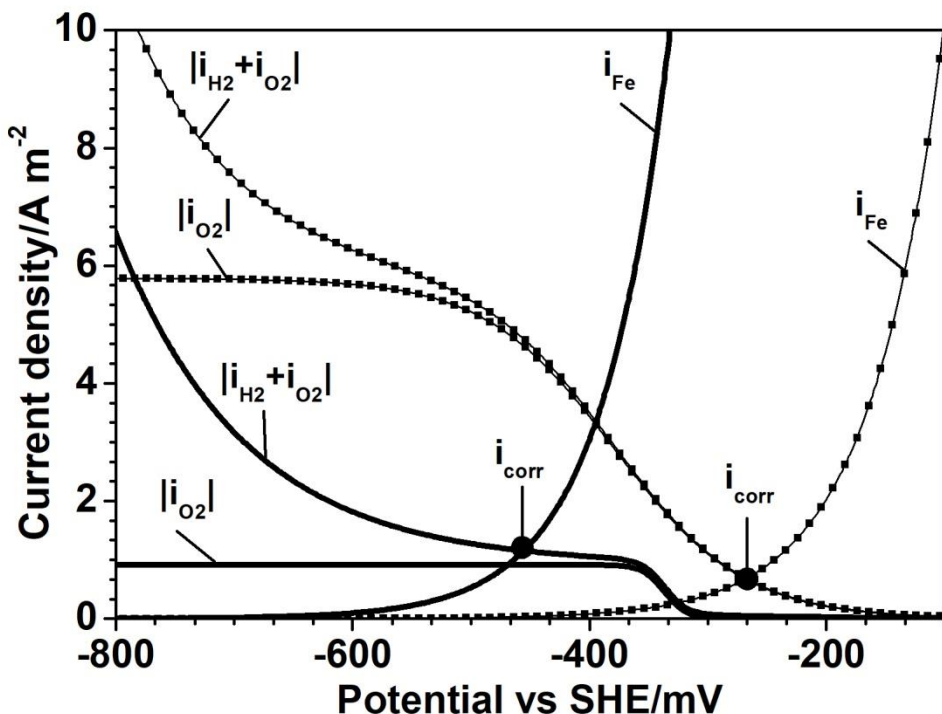


Figure 9. Partial polarization curves for carbon steel immersed in aerated 0.5 M LiBr measured in the AFC at initial time $t=0$ h (dotted line) and final time $t = 5$ h (solid line). The mixed potential theory (i.e., i_{corr}) can be observed at the intersection between the total anodic and cathodic curves

In this figure, the intersection between the polarization curves for anodic iron oxidation and the total curve for the cathodic ORR and HER represents the corrosion current density. In addition, it is seen that for the measurements under an oxide-free surface, the corrosion control regime is equivalent to the ORR under a mixed charge-transfer and diffusion regime, in contrast to an oxide-covered surface situation where an oxygen diffusion regime is combined with HER kinetics [23]. This parameter K is in accord with kinetic parameters obtained for the ORR where a mixed charge-transfer and diffusion regime is observed for the first two immersion hours.

3.5. Electrochemical impedance spectroscopy

The corrosion behavior of carbon steel immersed in aerated 0.5 M LiBr solution was evaluated via EIS at different immersion times. Fig. 10 shows the Nyquist and Bode plots obtained for carbon steel samples using the RDE and AFC electrochemical cells. Although the measured impedances for both electrochemical cells have almost identical plot shapes, the EIS results for the AFC are slightly higher than those for the RDE. This result suggests a higher resistance to the corrosion process caused by the lower flow rate in the AFC compared with the RDE, which agrees with the corrosion rate values obtained from the polarization curves (Table 1).

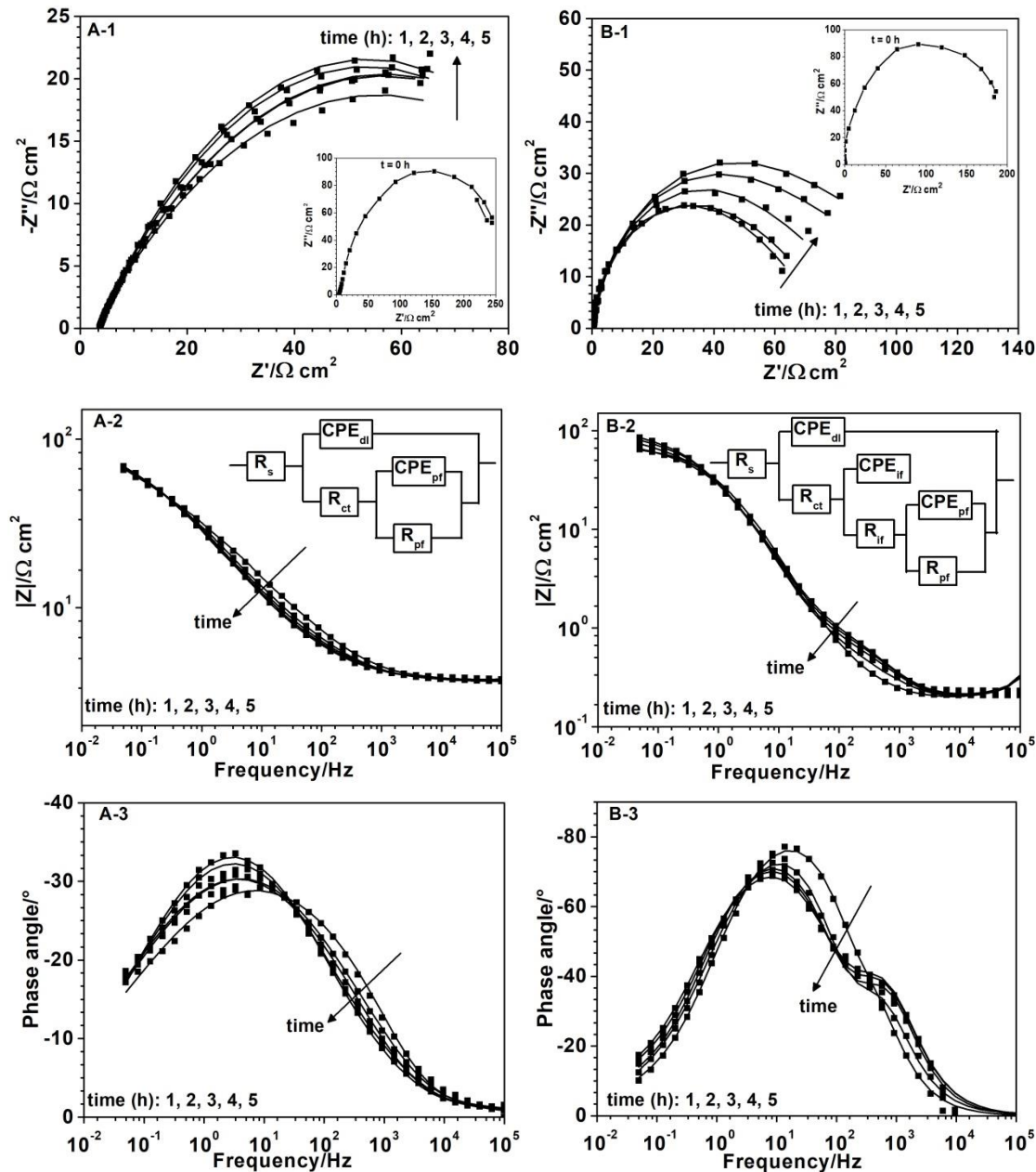


Figure 10. Impedance measurements for carbon steel immersed in an aerated 0.5 M LiBr solution using an RDE (A) and AFC (B) electrochemical cell. Time-dependent Nyquist (1) and Bode (2-3) plots. Comparison of experimental data (dotted line) and fitted data (solid line) using equivalent circuits models. Inset figure indicates the Nyquist plot for the initial impedance measurement of $t = 0 \text{ h}$ (A-1 and B-1 insets).

The results show an inductive loop at low frequencies principally observed during the first measurements (inset in Fig. 10A-1 and Fig. 10B-1), which is related to the adsorption of bromide ions, hydroxyl ions, and intermediate species, such as $(\text{FeOH})_{\text{ads}}$, formed during the dissolution of iron molecules [45]. Furthermore, the capacitive loops observed during EIS analysis suggest two or three time constants related to the oxide film deposited on the metallic surface due to the corrosion process, and their changes can be attributed to the transformation of the different oxide phases in the solid-liquid interface. In all cases, the Nyquist plot does not show perfect semicircles at low frequencies,

suggesting dispersion by the non-ideality of the surface and by the homogeneity and the mass transfer resistance [10, 46]. Additionally, the influence of the immersion time on the size of the capacitive loops in the Bode plot clearly indicates slight variations at high frequencies, in contrast with the capacitive loop at low frequencies, which increases in diameter with corrosion time. Among the different tested configurations for the equivalent circuit with two or three time constants, the circuits shown in Fig. 10A-2 and Fig. 10B-2 were the models with the best fits to the experimental data. In these equivalent circuits, the electrical elements were a solution resistance R_s , a time constant attributed to the double layer capacity and the charge transfer resistance at the oxide-surface interface (CPE_{dl}/R_{ct}), and a time constant for describing the diffusion of ionic ions and oxygen molecules through the porous corrosion film (CPE_{pf}/R_{pf}), such as that shown in Fig. 10A-2. For the AFC, the equivalent circuit shown in Fig. 10.B-2 includes a third time constant (CPE_{if}/R_{if}) that is used to describe a second process due to the transformation of the solid phase at the inner wall of the surface [46]. The CPE element was used as an inhomogeneity factor caused by surface roughness/porosity and a possible diffusional factor instead of a pure capacitor that is given by [10]:

$$Z_{CPE} = [Q(j2\pi f)^n]^{-1} \quad (8)$$

where Q is a CPE constant related to the electroactive species and surface, j is the imaginary unit, f is the frequency in Hz, and n is the CPE exponent, which varies between 0 and 1.

The experimental and fitted data are shown in Fig. 10 and the EIS parameter values for the equivalent circuit are tabulated in Table 2.

Table 2. EIS parameters of carbon steel in aerated 0.5 M LiBr for the AFC and RDE

Annular Flow Cell										
t (h)	R (Ω cm^2)	R_{ct} (Ω cm^2)	Q_{dl} (Ω^{-1} cm^{-2} s^n)	n_{dl}	R_{pf} (Ω cm^2)	Q_{pf} (Ω^{-1} cm^{-2} s^n)	n_{pf}	R_{if} (Ω cm^2)	Q_{if} (Ω^{-1} cm^{-2} s^n)	n_{if}
1	0.207	0.581	1.57×10^{-3}	1	37.32	1.57×10^{-2}	0.64	32.46	1.79×10^{-3}	0.94
2	0.210	0.673	1.83×10^{-3}	0.94	30.80	4.29×10^{-2}	0.68	45.24	2.80×10^{-3}	0.94
3	0.208	0.800	1.61×10^{-3}	0.92	43.88	3.07×10^{-2}	0.61	46.08	3.09×10^{-3}	0.94
4	0.213	0.780	1.13×10^{-3}	0.95	62.64	2.08×10^{-2}	0.50	44.73	3.70×10^{-3}	0.90
5	0.218	0.818	1.08×10^{-3}	0.95	66.20	1.92×10^{-2}	0.50	49.13	4.10×10^{-3}	0.87
Av.	0.211	0.73	1.44×10^{-3}	0.95	48.17	2.59×10^{-2}	0.59	43.53	3.1×10^{-3}	0.92

Rotating Disk Electrode							
t (h)	R (Ω cm^2)	R_{ct} (Ω cm^2)	Q_{dl} (Ω^{-1} cm^{-2} s^n)	n_{dl}	R_{pf} (Ω cm^2)	Q_{pf} (Ω^{-1} cm^{-2} s^n)	
1	3.716	0.025	8.26×10^{-5}	0.92	92.46	1.09×10^{-2}	0.46
2	3.533	0.047	9.28×10^{-5}	0.83	93.10	1.15×10^{-2}	0.48
3	3.466	0.100	1.14×10^{-6}	0.80	94.92	1.17×10^{-2}	0.50
4	3.390	0.209	1.00×10^{-6}	0.80	97.31	1.18×10^{-2}	0.51
5	3.338	0.295	1.17×10^{-6}	0.80	99.70	1.21×10^{-2}	0.52
Av.	3.488	0.135	3.57×10^{-5}	0.83	95.50	1.16×10^{-2}	0.50

Although the low values of n are related to the inhomogeneity of the surface, in this case its variability with the immersion time could indicate an activity increase of anodic sites as a result of the growing pits process promoted by the diffusion of bromide ions to the metallic surface, thus creating a rough surface. In this respect, the n_{dl} values reveal important differences between the electrochemical cells with average values of 0.95 and 0.83 for the AFC and RDE, respectively. These results indicate the presence of several pits sites when the RDE is used. Furthermore, the slight decrease in n_{pf} and n_{if} clearly show a contribution from the diffusion process of iron ions or oxygen molecules through the corrosion products film formed as a limiting stage [47].

As mentioned previously, during the immersion of carbon steel in LiBr solution, a decrease in the oxygen mass transport from the bulk solution to the metallic solution occurs due to the build-up of corrosion products on the metal surface that in turn produces an increase in the mass transfer resistance. In this context, the corrosion behavior of iron can be observed by the variations in the phase angle at low frequencies, where the limiting oxygen mass transfer observed in the AFC is signified by a higher phase angle (approximately 70°) compared with the phase angle for the RDE (approximately 30°). These results are in accord with the variations in the limiting current densities of both cells, as depicted in Table 1. This behavior, in conjunction with the continuous corrosion of carbon steel, promotes a high iron ion concentration close to the corrosion products/metallic surface interface, which is adsorbed on the early γ -FeOOH oxide phase. By increasing the immersion time, an important part of the oxide phase evolution is depicted by the formation of a new phase angle peak (at approximately 300 Hz), where the iron ions adsorbed on a lepidocrocite phase (γ -FeOOH) can be oxidized by the protons of water to form a magnetite phase (Fe_3O_4), indicating a framework of multi-layer evolution formation that occurs at pH > 7 [14, 48, 49].

Considering the oxide film deposited on the metallic surface, it is found that the resistance of the outer porous layer R_{pf} and inner oxide film R_{if} were higher by two and three orders of magnitude, respectively, compared with the charge transfer resistance (R_{ct}), suggesting the influential role of a diffusion phenomenon on the corrosion process. In particular, for the RDE, the increase in the oxide film resistance with time is principally associated with an increase in n_{pf} . This behavior explains the complex mechanism for the oxide phase transformation of Fe^{+2} to Fe^{+2}/Fe^{+3} oxides by the flow rate of oxygen, which agrees with the increase in the phase angle peak with the immersion time. This passive character of the oxide film caused by a competitive transformation of $Fe(OH)_2$ to Fe_3O_4 or γ -FeOOH [14, 31] is shown by the poor definition of the phase angle peak at 300 Hz, which is due to different local oxygen concentrations close to the metallic surface and in the porous oxide layer.

In this respect, a lower oxygen mass transfer and its contribution to the cathodic current density explains the differences between the Nyquist and Bode plots of the AFC and RDE cells. According to the values obtained by fitting the EIS curves, the capacitance of the double layer is higher in the AFC than in the RDE. This result can be further substantiated by the variations in $i_{0,H2}$, which were much larger for the AFC than for the RDE. Additionally, the results show that the increase in the phase angle peak at 300 Hz could be related to an increase in the passive properties of the oxide film. However, a contrary trend in the phase angle peak close to 10 Hz is observed, where the phase angle peak decreased with the immersion time. This means a continuous degradation of the oxide film, principally due to the transformation of the initial γ -FeOOH oxide phase to a Fe_3O_4 phase, which is primarily

caused by a higher concentration of ferrous ions in relation to the dissolved oxygen concentration, and by the large contribution of the water reduction reaction to the global corrosion behavior.

3.6. Morphological inspection

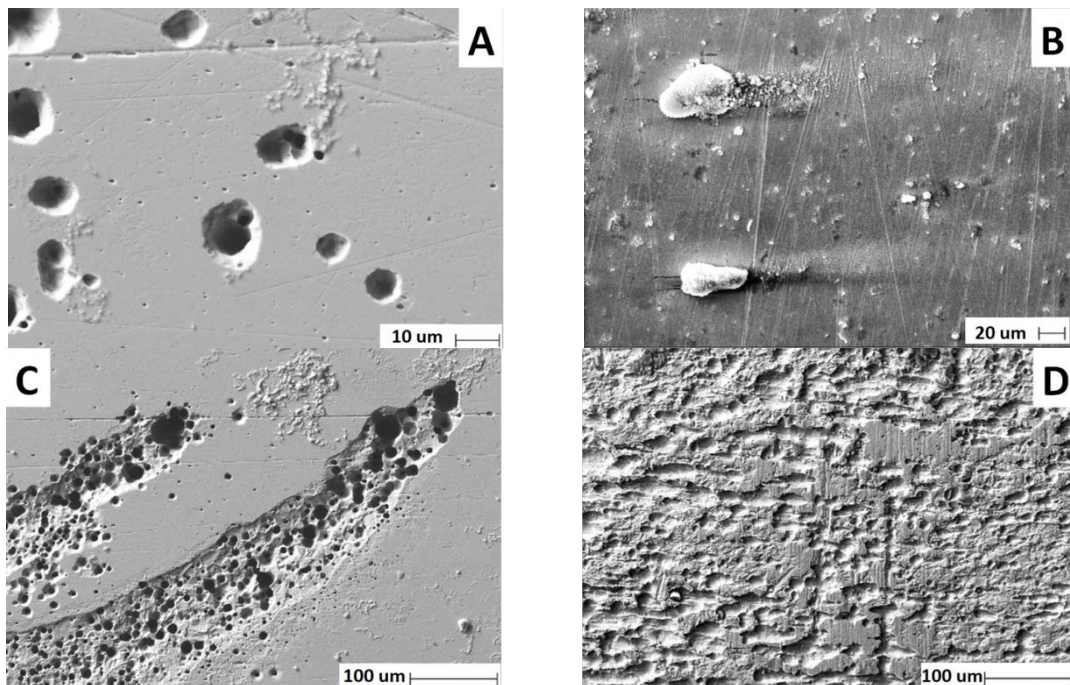


Figure 11. SEM micrographs of carbon steel samples after five hours of immersion in LiBr solution. Pit morphologies (A), influence of the flow direction on the corrosion products in the AFC (B), and pitting patterns in RDE (C) and AFC (D)

Fig. 11 shows images of carbon steel surfaces after five hours of immersion in aerated 0.5 M LiBr solution under different hydrodynamic conditions at the OCP. The presence of pits of different sizes confirms that pitting corrosion is the dominant corrosion mechanism on carbon steel in lithium bromide solutions. From Fig. 11A it is evident that pit shapes present diffuse borders with a lateral spread at the pit mouth and a large propagation from the pit center where a significant depth is observed, suggesting the high activity of bromide ions. The variations in the pit shape indicate different distributions of the pitting current density, which also changes with the immersion time and fluid flow pattern. In addition, Fig. 11A shows small pitting sites with hemispherical shape that can be related to a uniform current density distribution during the initial stage of the pit. These hemispherical pits change during the metastable growth where a high propagation is observed in relation to the lateral spread, promoting a high current density at the pit bottom. In this sense, and to maintain the electroneutrality, the bromide ions tend to migrate into the pits in the anodic sites, leading to a high bromide concentration close to the mouths of the pits. Additionally, for the AFC and RDE pitting patterns, a comet-tail morphology is found in larger pits, suggesting a continuous growth with aggressive solution pouring out of the cavities due to the fluid flow patterns (Figs. 3 and 11B). A comparative evaluation of the corroded samples for both electrochemical cell configurations observed

in Figs. 11C and 11D shows that the superficial distribution of the pits was highly dependent on the fluid flow pattern. A visual inspection of the color variations shows that the metal degradation was higher by lateral spread than by pitting propagation for the AFC, whereas the pitting propagation was higher than the lateral spread for the RDE.

The pitting corrosion occurrence is consistent with the OCP, LVS and EIS measurements represented by a continuous shift of potentials toward more negative values with immersion time, and by higher values of the capacitance (CPE_{pf} and CPE_{if}); indicating that bromide ions enhance the pit susceptibility of carbon steel with a pit morphology susceptible to the effect of local hydrodynamic conditions. In a previous study, we found a similar mode of pit propagation in LiBr that differs from that reported for chloride ions [21]. This high corrosion aggressiveness induced by bromide ions on iron oxidation is also confirmed from the $i_{0,Fe}$ values obtained by Cáceres [9] for the corrosion of carbon steel in 0.5 M NaCl solutions, which were 10-fold lower than those obtained in this work.

4. CONCLUSIONS

In this study, we investigated the corrosion behavior of carbon steel in a neutral 0.5 M LiBr aqueous solution using two different electrochemical cells, a rotating disk electrode and an annular flow cell with a cylindrical band electrode. In summary, the influence of the immersion time for both electrochemical cell arrangements is demonstrated by an increase in the corrosion rate followed by a maximum local value and a subsequent asymptotic decrease. These changes are strongly related to the formation and growth of magnetite and α -lepidocrocite as the main oxide phases promoting a sufficiently low oxygen concentration close to the metallic surface. Depending on the hydrodynamic conditions, the results demonstrated no variations in the iron regime with the immersion time; however, the cathodic ORR changes from a mixed charge-diffusion regimen to a pure diffusional regime after two more hours of immersion. Due to the interrelation between the ORR and HER, the cathodic behavior at the corrosion potential becomes a combination of the oxygen reduction mass transfer and hydrogen evolution kinetics. This combination was more pronounced at long immersion times and low fluid flows. The influence of the hydrodynamic conditions and the immersion time on the corrosion rate was corroborated using EIS measurements interpreted in terms of a synergistic effect between the oxygen mass transfer and iron oxide layer formation and growth. In turn, based on the morphological analysis, the bromide ion influence was supported by results from previous publications, where the bromide ion enhanced the pitting susceptibility from a combined influence of pitting propagation, a lateral spread, the electrochemical cell arrangements and the local hydrodynamic conditions.

ACKNOWLEDGMENTS

The authors acknowledge the financial support from the Comisión Nacional de Investigación Científica y Tecnológica CONICYT through the PAI Project N° 79150020 conducted at the Universidad de Atacama, Copiapó, Chile. L. Cáceres acknowledges financial support from CEBIB, Santiago, Chile.

References

1. K. Yazdanfar, X. Zhang, P.G. Keech, D.W. Shoesmith and J.C. Wren, *Corros. Sci.*, 52 (2010) 1297
2. L. Li, C. Wang and H. Lu, *Electrochim. Acta*, 104 (2013) 295
3. M.A.C. de Castro and B.E. Wilde, *Corros. Sci.*, 19 (1979) 923
4. C. Cuevas-Arteaga, J. Porcayo Calderon, C.F. Campos Sedano and J.A. Rodriguez, *Int. J. Electrochem. Sci.*, 7 (2012) 445
5. G. Kear, K. Bremhorst, S. Coles and S.H. Huáng, *Corros. Sci.*, 50 (2008) 1789
6. E. Heitz, DC Electrochemical Methods. In: P. Marcus and F. Mansfeld, Analytical Methods in Corrosion Science and Engineering, CRC Press Taylor & Francis Group, (2006) New York, USA
7. G.J. Offer, P. Shearing, J.I. Golbert, D.J.L. Brett, A. Atkinson and N.P. Brandon, *Electrochim. Acta*, 53 (2008) 7614
8. A. Soliz and L. Cáceres, *J. Electrochem. Soc.*, 162 (2015) C385
9. L. Cáceres, T. Vargas and L. Herrera, *Corros. Sci.*, 51 (2009) 971
10. H. Ashassi-Sorkhabi and E. Asghari, *Corros. Sci.*, 51 (2009) 1828
11. L. Wang, J. Wang and W. Hu, *Int. J. Electrochem. Sci.*, 13 (2018) 7356
12. M. Morcillo, I. Díaz, B. Chico, H. Cano and D. De la Fuente, *Corros. Sci.*, 83 (2014) 6
13. Y. Wang, G. Cheng, W. Wu, Q. Qiao, Y. Li and X. Li, *Appl. Surf. Sci.*, 349 (2015) 746
14. T. Misawa, K. Hashimoto and S. Shimodaira, *Corros. Sci.*, 14 (1974) 131
15. P. Refait, P. Girault, M. Jeannin and J. Rose, *Colloids Surf. A Physicochem. Eng. Asp.*, 332 (2009) 26
16. D.L.A. de Faria, S.V. Silva and M.T. de Oliveira, *J. Raman Spectrosc.*, 28 (1997) 873
17. K. Xiao, C. Dong, X. Li and F. Wang, *J. Iron Steel Res. Int.*, 15 (2008) 42
18. M. Stratmann and J. Müller, *Corros. Sci.*, 36 (1994) 327
19. W. Kuang, X. Wu and E.H. Han, *Corros. Sci.*, 63 (2012) 259
20. A. Davydov, K.V. Rybalka, L.A. Beketaeva, G.R. Engelhardt, P. Jayaweera and D.D. Macdonald, *Corros. Sci.*, 47 (2005) 195
21. A. Soliz and L. Cáceres, *Int. J. Electrochem. Sci.*, 10 (2015) 5673
22. J.A. Bard and R.L. Faulkner, Electrochemical Methods: Fundamentals and Applications, Wiley, (2001) New York, USA
23. H. Kaesche, Corrosion of metals. Physicochemical Principles and Current Problems, Springer, (2003) New York, USA
24. C. Wagner and W. Traud, *Z. Elektrochem. Bd.*, 44 (1938) 391
25. S. Xu, Y. Kim, D. Higgins, M. Yusuf, T.F. Jaramillo, and F.B. Prinz, *Electrochim. Acta*, 255 (2017) 99
26. D. Covello and I.G. Casella, *Electrochim. Acta*, 261 (2018) 104
27. G. Berthome, B. Malki and B. Baroux, *Corros. Sci.*, 48 (2006) 2432
28. M. Hashimoto, S. Miyajima and T. Murata, *Corros. Sci.*, 33 (1992) 885
29. W. Wu, Z. Liu, S. Hu, X. Li and C. Du, *Ocean Eng.*, 146 (2017) 311
30. L. Cáceres, T. Vargas and M. Parra, *Electrochim. Acta*, 54 (2009) 7435
31. H. El Hajj, A. Abdelouas, Y. El Mendili, G. Karakurt, B. Grambow and C. Martin, *Corros. Sci.*, 76 (2013) 432
32. P. Allen and N.A. Hampon, *Surf. Technol.*, 7 (1978) 273
33. Y. El Mendili, A. Abdelouas and J.F. Bardeau, *Phys. Chem. Chem. Phys.*, 15 (2013) 9197
34. N.R. Smart, D.J. Blackwood and L. Werme, *Corrosion*, 58 (2002) 547
35. H. Tamura, *Corros. Sci.*, 50 (2008) 1872
36. M. Stratmann, K. Bohnenkamp and H.J. Engell, *Corros. Sci.*, 23 (1983) 968
37. W. Shi, Z.H. Dong, D.J. Kong and X.P. Guo, *Cement Concrete Res.*, 48 (2013) 25
38. M. Hanesch, *Geophys. J. Int.*, 177 (2009) 941

39. M. Yamashita, H. Nagano, T. Misawa and H.E. Townsend, *ISIJ International*, 38 (1998) 285
40. D.D. Macdonald, *Electrochim. Acta*, 56 (2011) 1761
41. B. Krishnamurthy, R.E. White and H.J. Ploehn, *Electrochim. Acta*, 46 (2001) 3387
42. L. Cáceres, A. Soliz and T. Vargas, *J. Electrochem. Soc.*, 163 (2016) C171
43. A.Y. Musa, A.A.H. Kadhum and A.B. Muhamad, *Int. J. Electrochem. Sci.*, 5 (2010) 1911
44. U.K Ghosh and S.N. Upadhyay, *AIChE J.*, 31 (1985) 1721
45. F. Farelas, M. Galicia, B. Brown, S. Nesic and H. Castaneda, *Corros. Sci.*, 52 (2010) 509
46. R. Cabrera-Sierra, E. Sosa, M.T. Oropesa and I. González, *Electrochim. Acta*, 47 (2002) 2149
47. M.B. Valcarce and M. Vazquez, *Electrochim. Acta*, 53 (2008) 5007
48. Y. Tamaura, K. Ito and T. Katsura, *J. Chem. Soc. Dalton Trans.*, 1 (1983) 189
49. Y.H. Huang and T.C. Zhang, *Water Research*, 39 (2005) 1751

Appendix A

Hydrodynamic characterizations of the RDE and AFC were obtained by solving the Navier-Stokes equation [42] assuming a time independent flow profile, an incompressible fluid, and a negligible external force:

$$\rho(u \cdot \nabla)u = \nabla \cdot [-pI + \mu(\nabla u + (\nabla u)^T)] \quad (A1)$$

$$\rho \nabla \cdot u = 0 \quad (A2)$$

where ρ is the solution density, u is the flow velocity field of the solution, p is the pressure, and I is the identity matrix.

The flow regime was laminar to transient for both electrochemical cells (i.e., $1900 < Re < 2700$), and we assumed that the fluid flow does not lose stability at $Re=2700$ and that the undulations are negligible close to the metallic surface maintaining a fully developed profile [8]. Then, a laminar flow can be considered.

Equations A1 and A2 were solved numerically using the commercial software COMSOL Multiphysics (5.2). 2D axisymmetric and 3D models were used for the RDE and AFC, respectively. The domain simulation was configured with 655144 tetrahedral and 52506 triangular elements for the AFC, and 7331 triangular and 2425 quadrilateral elements for the RDE.

Fig. 7 compares the distribution of the wall shear stress calculated for a flow rate of 1.29 L min^{-1} and an angular velocity of $2500 \text{ rev min}^{-1}$ for the AFC and RDE, respectively. From the figure, a linear increase in the shear stress with the radius is observed for the RDE, which agrees with the theoretical shear stress determined by solving the shear tensor terms according to the von Karman and Cochran

treatment [42]. Furthermore, for the AFC cell no large variations in the wall shear stress were observed throughout the length of the inner surface, maintaining a constant value of approximately 2 Pa. This wall shear stress of the AFC is smaller than those of the RDE, which vary up to 10 Pa for a working electrode radius of 3 mm and up to 18 Pa for a plastic rod radius of 6 mm.

© 2018 The Authors. Published by ESG (www.electrochemsci.org). This article is an open access article distributed under the terms and conditions of the Creative Commons Attribution license (<http://creativecommons.org/licenses/by/4.0/>).